HHS Public Access

Author manuscript

J Am Chem Soc. Author manuscript; available in PMC 2022 June 11.

Published in final edited form as:

J Am Chem Soc. 2022 April 20; 144(15): 6839–6850. doi:10.1021/jacs.2c00973.

A pH- and Calcium-Dependent Aromatic Network in the SARS-CoV-2 Envelope Protein

João Medeiros-Silva, **Noah H Somberg**, **Harrison K. Wang**, **Matthew J. McKay**, **Venkata S. Mandala**, **Aurelio J. Dregni**, **Mei Hong***

Department of Chemistry, Massachusetts Institute of Technology, 170 Albany Street, Cambridge, MA 02139

Abstract

The envelope (E) protein of the SARS-CoV-2 virus is a membrane-bound viroporin that conducts cations across the endoplasmic reticulum Golgi intermediate compartment (ERGIC) membrane of the host cell to cause virus pathogenicity. The structure of the closed state of E transmembrane (TM) domain, ETM, was recently determined using solid-state NMR spectroscopy. However, how the channel pore opens to allow cation transport is unclear. Here we use ^{13}C and ^{19}F solid-state NMR to investigate the conformation and dynamics of ETM at acidic pH and in the presence of calcium ions, which mimic the ERGIC and lysosomal environment experienced by E in the cell. Acidic pH and calcium ions increased the conformational disorder of the N- and C-terminal residues and increased the water accessibility of the protein, indicating that the pore lumen has become more spacious. ETM contains three regularly spaced phenylalanine (Phe) residues in the center of the peptide. ^{19}F NMR spectra of para-fluorinated Phe20 and Phe26 indicate that both residues exhibit two sidechain conformations, which coexist within each channel. These two Phe conformations differ in their water accessibility, lipid contact and dynamics. Channel opening by acidic pH and Ca^{2+} increases the population of the dynamic lipid-facing conformation. These results suggest an intricate aromatic network that regulates the opening of the ETM channel pore. This aromatic network may be a target for E inhibitors against SARS-CoV-2 and related coronaviruses.

Graphical Abstract

*Corresponding author: Professor Mei Hong, meihong@mit.edu.

Supporting Information Available

Tables of NMR samples and experimental parameters, figures of 2D NC and CC spectra of ETM under different pH and calcium concentrations, water-edited ^{13}C spectra, 2D FF spectra and cross peak intensity analysis, 2D HF and HC spectra, MALDI-MS and solution NMR data, and summary of experimental pulse diagrams. This material is available free of charge via the Internet at http://pubs.acs.org.

The authors declare no competing financial interest.

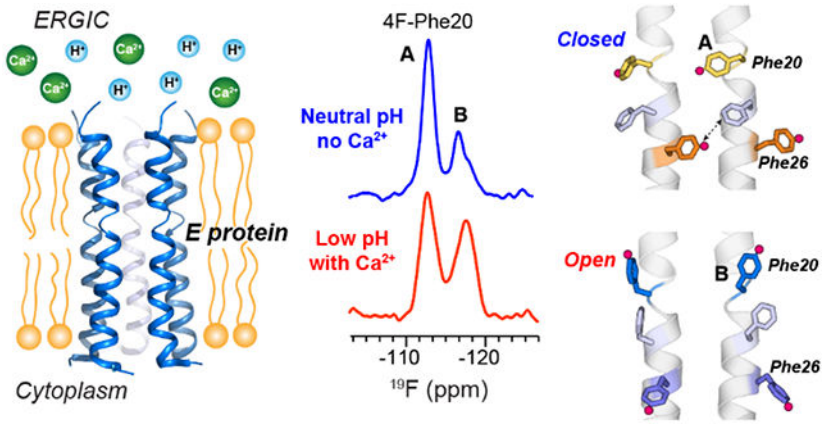

Keywords

Solid-state NMR; COVID-19; viroporins; ^{19}F chemical shift; membrane proteins

Introduction

The Severe Acute Respiratory Syndrome Coronavirus 2 (SARS-CoV-2) that is the causative agent of the COVID-19 pandemic contains four structural proteins: the spike protein (S), the membrane protein (M), the envelope protein (E), and the nucleocapsid protein (N). Among these, E is involved in virus assembly and budding, interacts with host and virus proteins, and acts as an ion channel that alters the ionic balance of the host cell and the virus[1–3]. The cytoplasmic domain of E mediates its interaction with other virus and host proteins, including M[4–5], syntenin-1[6] and PALS1[7–9], while the transmembrane (TM) domain mediates cation conduction. E carries out these functions in the membrane of the endoplasmic reticulum Golgi intermediate compartment (ERGIC). Here E assembles into an ion channel that conducts Na^+, K^+, Ca^{2+} and Mg^{2+} in a pH-dependent manner[10–13] (Fig. 1). This cation channel activity has been measured using electrophysiology in whole cells and single-channel voltage clamp experiments in planar bilayers. Expression of E in *Xenopus* oocytes and HEK293 cells showed cation-selective current that increased at acidic pH and that can be blocked by inhibitors such as hexamethylene amiloride (HMA) and amantadine[12, 14–15]. Consistent results were obtained in planar bilayers, where acidic pH increased the conductance and open probability of E[13]. Planar bilayer experiments also showed that the K^+ and Na^+ selectivity of E is affected by pH, anionic lipids, and calcium[11, 13, 16–17]. This pH-dependent channel activity of E is relevant because the ERGIC lumen is mildly acidic (pH 6–7)[18] and SARS-CoV-2 was recently found to use the highly acidic lysosome (pH 4.2–5.2) to egress[19].

Importantly, the E-provoked Ca^{2+} and H^+ imbalance in cells induces endoplasmic reticulum stress, NLRP3 inflammasome activation, and excessive secretion of inflammatory cytokines[11, 13, 20]. These pathogenic effects have been demonstrated in cell and animal models, where E alone induced cell death and acute respiratory distress syndrome in mice[13]. Administration of E inhibitors reduced the levels of inflammatory cytokines and SARS-CoV-2 titers, thus E is a promising antiviral drug candidate for treating COVID-19[13, 22–23].

Similar symptom-alleviating effects derived from the impairment of E have also been reported for SARS-CoV-1, which shares the same TM amino acid sequence as SARS-CoV-2[24–25]. Engineered viruses lacking the E gene could potentially be employed as live attenuated vaccines, similar to what was proposed for the influenza A virus lacking the M2 (AM2) protein[26].

Despite the importance of E's cation channel activity for SARS-CoV-2 pathogenicity, molecular-level structural information about the mechanism with which the E channel opens to allow cation transport is still scarce. This structural information is important for designing E inhibitors as antiviral drugs against SARS-CoV-2 infections. The transmembrane domain of E (ETM) spans approximately residues 8–38[27], and is well conserved across SARS-CoV-2 variants[28–30]. ETM can be compared to the TM domain of the best studied viroporin, the influenza A virus M2 protein (AM2). M2 exhibits proton channel activities to acidify the virion during influenza uncoating and to increase the pH of the Golgi apparatus[31–34]. The same drugs that are active against E[35–37], including amantadine and HMA, also inhibit AM2's proton channel activity[38–41], which in turn halt the influenza cycle.

Recently, we determined the closed structure of ETM bound to ERGIC-mimetic lipid bilayers using solid-state nuclear magnetic resonance (NMR) spectroscopy (Fig. 1c)[42]. The structure, solved at neutral pH in the absence of calcium, shows a rigid and tight pentameric helical bundle whose pore is occupied by predominantly hydrophobic residues except for a polar asparagine (Asn15). How this tight pore opens to conduct cations is so far unknown. Interestingly, three regularly spaced Phe residues in the middle of the TM segment (Fig. 1a) stack to bridge the helix-helix interface. This led to the hypothesis that these aromatic residues might be important for regulating the opening of the ETM pore.

Here we present a solid-state NMR study of ETM bound to ERGIC-mimetic lipid bilayers at acidic pH in the presence of calcium ions. We show that both cations significantly increase the water accessibility of the channel, indicating a widening of the pore lumen. Unexpectedly, ^{19}F NMR spectra of singly Phe-fluorinated ETM revealed two sidechain conformations at both Phe20 and Phe26. The populations of these two conformations change between the closed and open states. These results suggest an aromatic network whose structures correlate with the open and closed states of the channel. These structural insights may be useful for the development of E inhibitors against SARS-CoV-2.

Materials and Methods

Expression and purification of ^{13}C, ^{15}N-labeled ETM

^{13}C, ^{15}N-labeled ETM, which spans residues 8–38 of the full-length protein (Fig. 1a), was expressed and purified as described previously[42]. Briefly, *E. coli* BL21 (DE3) cells were transformed using a Champion pET-SUMO plasmid carrying the gene of SARS-CoV-2 ETM fused to a His_6-SUMO tag. Cells were grown at 37°C in ^{13}C, ^{15}N-labeled M9 media containing 3 g/L of $^{13}C_6$-D-glucose and 1 g/L of ^{15}N-labeled NH_4Cl. When cell cultures reached an OD_{600} of 0.9, His_6-SUMO-ETM fusion protein expression was induced with 0.8 mM IPTG for 16 h at 18°C. Cells were harvested, suspended in lysis buffer (50 mM Tris pH 8, 100 mM NaCl, 1 mM $MgSO_4$) and treated with 0.5 mg/mL lysozyme, 1%

Triton-X and benzonase nuclease (Millipore). Lysis was carried out by sonication on ice, the cell debris was removed and the extract was incubated with Ni^{2+} Profinity IMAC resin (Biorad). Impurities were washed out using 30 mM imidazole, and His_6-SUMO-ETM was eluted at 250 mM imidazole in 50 mM Tris buffer (pH 8, 100 mM NaCl, 0.1% n-dodecyl-B-D-maltoside (DDM)). The eluted His_6-SUMO-ETM fractions were diluted to ≤80 mM imidazole and treated with 0.5 mg/mL SUMO protease and 5 mM tris(2-carboxyethyl)phosphine (TCEP) for 2 h at 20°C with gentle rocking. Recombinant ETM was purified by reverse-phase HPLC on a Varian Prostar 210 System using an Agilent C3 column (21.2 mm × 150 mm, 5 μm particle size) with a linear gradient of 5–99% 9:1 ACN : IPA with 0.1% TFA (channel B) at a flow rate of 10 mL/min (channel A is water with 0.1% TFA) at room temperature. To increase the purification yield, we recovered His_6-SUMO-ETM aggregates from the Ni^{2+} affinity column, aggregates formed during SUMO protease cleavage, and residual uncleaved SUMO-ETM from the first round of HPLC. The combined material was pooled in 9 : 1 ACN : IPA solution with 0.1% TFA and the organic solvents were evaporated. The material was redissolved in lysis buffer containing Triton-X and re-purified by Ni^{2+} column and HPLC. The final yield was ~14 mg ^{13}C, ^{15}N-labeled ETM per liter of M9 culture.

Synthesis of 4-^{19}F-Phe labeled ETM peptides

ETM peptides with either a 4-^{19}F-Phe20 (4F-Phe20) label or a 4-^{19}F-Phe26 (4F-Phe26) label were synthesized using Fmoc solid-phase chemistry. Fmoc-4F-L-Phe was purchased from ChemImpex. The synthesis was carried out on a custom-built flow synthesizer[43]. H-Rink amide ChemMatrix® resin at 0.050 mmol (0.10 g at 0.5 mmol/g loading size) was loaded into the reactor, which was kept at 70°C. Amino acids were dissolved in HATU solution (2.5 mL per residue, 0.38 M in DMF, 9.5 eq). Immediately before each amino acid was coupled, DIEA (348 uL, 2.0 mmol, 20 eq) was added. All amino acids were coupled in ten-fold excess (1.0 mmol) for 45 s. To reduce single-residue deletion impurities, double coupling was performed at I13, V14, ^{18}LLFL^{21,23}FVVFLL^{28}, and R38. Each residue was deprotected with 20% piperidine in DMF solution for 25 s. After the final coupling step, the resin was dried, and the peptide was deprotected and cleaved from the resin using 5 mL TFA / phenol / water / TIPS solution (88 : 5 : 5 : 2 by volume) for 2 h. The resin was filtered off, the crude peptide was precipitated from the cleavage solution with cold 1:1 v/v hexane : diethyl ether, then washed twice with cold diethyl ether before being dried under vacuum overnight at room temperature. The resulting crude peptide was dissolved in trifluoroethanol (TFE) and purified by preparative reverse-phase HPLC using a Vydac C4 column (22 mm × 250 mm, 10 μm particle size) and a linear gradient of 80–100% methanol (channel B) over 25 min at a flow rate of 10 mL/min (channel A is water). The peptide was eluted at ~99% methanol. Fractions containing the peptide were assessed for relative purity by MALDI-MS and confirmed by ^{19}F solution NMR (Fig. S1a,b). The total yield of the synthesis and purification was ~2%.

Preparation of proteoliposome samples

Purified ETM peptides were reconstituted into an ERGIC-mimetic lipid membrane[10], which contains 45 : 20 : 13 : 7 : 15 molar ratios of 1-palmitoyl-2-oleoyl-sn-glycero-3-phosphocholine (POPC), 1-palmitoyl-2-oleoyl-sn-glycero-3-phosphoethanolamine (POPE),

L-α-phosphatidylinositol (PI), 1-palmitoyl-2-oleoyl-sn-glycero-3-phospho-L-serine (POPS) and cholesterol. Lipids were purchased from Avanti Polar Lipids, and dissolved in a 1:1 chloroform : methanol solution. ETM was dissolved in TFE and mixed with the lipid solution at the desired protein-lipid molar ratio (P/L). Most of the fluorinated ETM membrane samples were prepared at a P/L of 1:9, whereas ^{13}C, ^{15}N-labeled ETM samples were prepared at P/L ratios of 1:15 to 1:25 (Table S1). The protein-lipid mixture was concentrated under a stream of nitrogen gas and lyophilized to a dry homogenous film. Proteoliposomes were formed by suspending the film in the appropriate buffer under vigorous mixing and hydrating for 60 min. The suspension underwent 10 freeze/thaw cycles between liquid nitrogen and a 45°C water bath. The vesicle solution was ultracentrifuged at 250,000 × *g* using a Beckman SW60 Ti swinging-bucket rotor, and the resulting membrane pellet was dried in a desiccator until the pellet mass reaches 40% (w/w) water relative to total mass. The proteoliposome was then packed into 3.2 mm or 1.9 mm MAS rotors.

Four buffers were used to investigate the response of ETM to ionic conditions (Table S1). A pH 7.5 buffer containing 30 mM Tris-HCl, 30 mM NaCl, 1.5 mM EDTA and 0.15 mM NaN_3 was used to produce the closed state of ETM. The second solution involves the same pH 7.5 buffer but without EDTA and with additional 30 mM $CaCl_2$. This buffer probes the response of ETM to calcium binding. The third solution involves a pH 4.5 buffer consisting of 30 mM sodium acetate, 10 mM NaCl and 0.15 mM NaN_3. This condition probes the effects of acidic pH on ETM structure. The fourth solution involves the pH 4.5 buffer with additional 30 mM $CaCl_2$. Most of the NMR spectra on the open state of ETM were measured in the pH 4.5 buffer with calcium. The choice of acetate for the low-pH buffers minimizes pH variations after reconstitution of ETM into the membrane. We chose 30 mM Ca^{2+}, which is a higher concentration than the cellular Ca^{2+} concentrations of 100 nM to 0.4 mM, in order to ensure sufficient calcium ions are available to interact with and saturate the protein, since calcium ions also bind phospholipid headgroups, which are present at much higher concentrations in the NMR samples than in the cell.

To verify that the ETM conformation is unperturbed by the incorporation of 4F-Phe labels, we compared the ^{13}C chemicals shifts of ^{13}C, ^{15}N-labeled ETM with mixed ^{19}F- and ^{13}C,^{15}N-labeled ETM. We did not detect significant chemical shift perturbations, confirming that the 4F-Phe label does not perturb the protein (Fig. S2).

Solid-state NMR spectroscopy

^{13}C and ^{15}N solid-state NMR experiments were conducted on a Bruker Avance II 800 MHz (18.8 T) spectrometer using a BlackFox 3.2 mm HCN magic-angle-spinning (MAS) probe. These spectra are supplemented with spectra measured on an Avance 900 MHz (21.1 T) spectrometer using a Bruker 3.2 mm Efree HCN MAS probe. All ^{19}F MAS NMR spectra were recorded on an Avance III HD 600 MHz (14.1 T) spectrometer using a Bruker 1.9 mm HFX probe.

^{13}C chemical shifts were externally referenced to the adamantane CH_2 chemical shift at 38.48 ppm on the TMS scale. ^{15}N chemical shifts were referenced to the ^{15}N peak of ^{15}N-acetylvaline at 122.0 ppm on the liquid ammonia scale. ^{19}F chemical shifts were referenced to the ^{19}F peak of 5-^{19}F-tryptophan at −122.1 ppm on the CF_3Cl scale. The ^{1}H chemical

shift were referenced internally to the POPC Hγ chemical shift at 3.264 ppm on the TMS scale. The reported sample temperatures were estimated based on the ^{1}H chemical shift of bulk water[44].

2D ^{15}N-^{13}C and ^{13}C-^{13}C correlation spectra were measured on the 800 MHz spectrometer at 10.5 kHz MAS and a sample temperature of 293 K (Table S2). ^{15}N-^{13}Cα (NCα) polarization transfer was achieved using the SPECIFIC-CP sequence[45] with a 6 ms contact time. 2D ^{13}C-^{13}C correlation spectra were measured using 23 ms CORD mixing[46]. Water-edited 1D ^{13}C cross-polarization (CP) spectra and 2D NCα spectra were measured using a water-selective ^{1}H Hahn echo that consists of a 952 μs (i.e. 10 rotor periods) Gaussian 180° pulse and a pair of 95 μs delays, for a total echo duration of 1.14 ms[47] (Fig. S3). This ^{1}H T_2 period was followed by a variable spin diffusion mixing period to transfer the water ^{1}H polarization to the protein protons.

All ^{19}F MAS experiments, including 1D ^{19}F direct polarization (DP) and CP, 2D ^{19}F-^{19}F spin diffusion, and 2D ^{1}H-^{19}F and ^{13}C-^{19}F heteronuclear correlation (HETCOR) experiments, were conducted on the 600 MHz spectrometer at a sample temperature of 290 K. 1D ^{19}F CP and DP spectra were measured with recycle delays of 2 s and 8 s to detect the signals of rigid fluorines and all fluorines, respectively. The 2D ^{13}C-^{19}F HETCOR experiment was conducted with ^{19}F direct detection with 6–7 ms ^{13}C-^{19}F CP for polarization transfer. 2D ^{19}F-^{19}F spectra were measured at 38 kHz MAS with PDSD mixing and at 26 kHz MAS with CORD mixing.

^{1}H T_2-filtered 2D ^{1}H-^{19}F and ^{1}H-^{13}C HETCOR spectra were measured under 14 kHz MAS. The T_2 filter consisted of Hahn echo with a hard 180° pulse and a pair of 0.57 ms delays (8 rotor periods) for a total period of 1.14 ms. This selects the ^{1}H magnetization of water and mobile lipids while suppressing the magnetization of the protein. The water and lipid ^{1}H magnetization was then transferred to the protein using 100 ms ^{1}H mixing, followed by CP to ^{13}C or ^{19}F for detection. Solution state 1D ^{19}F NMR spectra were measured on a 600 MHz NMR spectrometer at 293 K. The chemical shifts were internally referenced to the TFA signal at −76.3 ppm.

NMR spectral analysis

All MAS NMR spectra were processed using TopSpin 3.5, and chemical shift assignment was conducted in NMRFAM-SPARKY 1.4 {Lee, 2015 #127}. Typical processing used either QSINE apodization with SSB = 3, or Gaussian apodization with LB = −20 Hz and GB = 0.05. 2D correlation spectra were plotted with a scaling factor of 1.2 between successive contour lines. All curve fittings were performed in GraphPad Prism.

The water accessibility values, S/S_0, were obtained from the intensity ratio of the S and S_0 spectra. For 1D spectra, the S/S_0 values were obtained from the integrated intensities of the Cα region (70–45 ppm) and sidechain region (45–10 ppm). For 2D spectra, the S/S_0 values were obtained from the integrated intensities of each correlation peak. Water-transferred buildup curves were obtained from 1D ^{15}N-filtered Cα spectra and 1D ^{1}H-^{13}C CP spectra and were normalized by the equilibrated intensities. Signal loss due to water ^{1}H T_1 relaxation during the spin diffusion mixing times was corrected by dividing the S/S_0

values by $e^{-t/T1}$, where the T_1 value was measured using the inversion recovery experiment. The error bar ε of the S/S_0 values was propagated from the signal-to-noise ratios (SNR) of the S and S_0 spectra using the equation $\varepsilon = (S/S_0)\left[\left(SNR_S^{-2} + SNR_{S_0}^{-2}\right)\right]^{1/2}$.

Hydration maps for water-edited 2D NCα spectra were calculated using a Python script[47–48]. Intensities of the 9 ms and 100 ms spin diffusion spectra were exported to the NMRglue package[49] and scaled by the number of scans. The spectra were noise-filtered by setting to 0 any peak intensities lower than 3.5 times the average noise level, which was estimated from a signal-free region of the spectrum. The intensities of the 9 ms and 100 ms spectra were then divided and plotted at contour levels between 0.002 and 0.5 in increments of 0.002. The water-peptide and lipid-peptide cross peak intensities were extracted from the integrated intensities of the water and lipid CH_2 cross sections at 4.8 ppm and 1.3 ppm, respectively in the 2D ^{1}H-^{19}F and ^{1}H-^{13}C HETCOR spectra.

Phe20 A-B ^{19}F-^{19}F distances were estimated from the 2D ^{19}F-^{19}F spin-diffusion rate k_{SD} using the following equation[50]:

$$k_{SD}\Delta\delta^2 = \frac{1.0 \times 10^{14} \text{Å}^6 s^{-3}}{r^6} \quad (1)$$

where $\Delta\delta_{AB}$ is the ^{19}F chemical shift difference between peaks A and B (5 ppm × 2π × 564 MHz for Phe20). The rate k_{SD} was obtained from the buildup curve of the normalized B-A cross-peak intensities according to

$$\frac{I_{BA}}{I_{BA} + I_{BB}} = \frac{1}{n}\left(1 - e^{-k_{SD}t_{mix}}\right) \quad (2)$$

Here t_{mix} is the ^{19}F spin diffusion mixing time, n is the number of inequivalent fluorines in the spin system, and I_{BA} and I_{BB} are the B-A cross peak intensity and B-B diagonal intensity.

Results

SARS-CoV-2 ETM channel opens at acidic pH in the presence of Ca^{2+}

The SARS-CoV-2 virion assembles in the ERGIC, which is mildly acidic (pH 6–7) and rich in calcium ions (0.4 mM Ca^{2+}) compared to the cytoplasm (100 nM Ca^{2+})[3, 51–53]. Recent studies found that SARS-CoV-2 egresses through the highly acidic lysosome (pH 4.2–5.2) instead of the biosynthetic secretory pathway[19]. Thus, it is important to understand the conformation and dynamics of E at acidic pH and under high Ca^{2+} concentrations. We chose pH 4.5 to mimic the lysosomal pH and 30 mM Ca^{2+} to allow sufficient free Ca^{2+} ions to interact with the ETM channel. In typical ~40% hydrated membranes used for solid-state NMR experiments, the lipid concentration is ~1.5 M, compared to the lipid concentration of ~0.10 M in an ERGIC compartment with a diameter of ~150 nm. Normalized by these lipid concentrations, 30 mM Ca^{2+} is about 5-fold excess compared to the ERGIC lumen Ca^{2+} level of 0.4 mM. This moderate excess compensates for other Ca^{2+} binding species such as buffer ions, to ensure that there is sufficient Ca^{2+} to saturate the ETM channel. This Ca^{2+}

concentration is within the range of 15 to 150 mM Ca^{2+} used in single-channel recordings of the E current[11 13].

We expressed and purified ^{13}C,^{15}N-labeled ETM from *E. coli* and reconstituted it into an ERGIC-mimetic lipid bilayer that contains phosphocholine, phosphoethanolamine, phosphatidylinositol, phosphoserine and cholesterol. Fig. 2a compares the 2D NCα spectra of membrane-bound ETM at pH 4.5 with calcium versus at neutral pH without calcium. The chemical shifts of most hydrophobic residues in the center of the peptide agree well between the two samples, indicating that the backbone conformation of the hydrophobic center of the TM domain is little affected by acidic pH and calcium. However, N-terminal and C-terminal residues such as T11, L12, I13, T35, L37, and R38 show noticeable chemical shift perturbations (CSPs). Moreover, T9, T11, L12 and R38 peak intensities are suppressed, indicating that these residues become more dynamic in the presence of calcium and at acidic pH. 2D ^{13}C-^{13}C correlation spectra (Fig. S4) confirm these observations, showing that the terminal residues' intensities are attenuated by acidic pH and calcium.

To investigate how the ETM channel lumen responds to acidic pH and calcium ions, we measured the water accessibility of the protein using the water-edited 2D NCα experiment. The experiment selects the water ^1H magnetization and transfers it to the protein amide protons for detection (Fig. S3b, d). Water-accessible residues exhibit higher intensities than dehydrated residues[48, 54–55]. By comparing the water-transferred intensities at a short mixing time and a long mixing time when the magnetization is equilibrated, we obtain information about the water accessibilities of the amino acid residues under different ionic conditions. Therefore, this water-edited NMR experiment provides information about the hydration and spaciousness of the ETM pore, but do not probe cation transport or cation selectivity. In this study, we refer to the more water-accessible state at acidic pH with calcium as the open state. Fig. 2b shows the water-transferred 2D NCα spectra of the neutral pH sample and the low-pH Ca^{2+}-bound sample. Contour lines represent the intensity ratios of spectra measured with 9 ms (S) and 100 ms (S_0) ^1H spin diffusion. The water-transferred intensities are larger for the low-pH Ca^{2+}-bound sample than for the neutral-pH Ca^{2+}-free sample. N-terminal residues such as V14, N15, and S16 and C-terminal residues such as A36 and L37 show higher water-transferred intensities than residues in the middle of the TM domain (Fig. 2c). The residue-specific hydration gradient correlates with the CSP profile, indicating that acidic pH and calcium ions both affect the conformation and increase the water accessibilities of the two termini of the TM peptide. A particularly well hydrated residue is N15, which is conserved among SARS and MERS viruses and which is thought to be important for E's cation conduction[3]. Water-transferred 1D ^{13}C NMR spectra measured as a function of mixing time (Fig. 2d, Fig. S5) are consistent with the 2D spectra, and show that the water-to-protein magnetization transfer intensities rise faster at low pH with Ca^{2+}-bound than at neutral pH without Ca^{2+} (Fig. 2e). When ETM was subjected to either acidic pH or calcium ions, the NCα and CC spectra show similar chemical shifts as when both cations are present (Fig. S4). Consistently, either calcium or acidic pH already accelerates water magnetization transfer to the protein (Fig. 2e). These results indicate that both acidic pH and calcium increase the water accessibilities of the ETM channel, and both conditions also increase the dynamics of the terminal residues.

Phe20 and Phe26 exhibit two sidechain conformations

The E protein contains three Phe's, spaced every three residues apart, in the center of the TM domain (Fig. 3a). The spacing by approximately one helical turn makes these Phe's prime targets for π-π stacking interactions. To investigate whether the Phe sidechain structures change between the neutral-pH closed state and the low-pH open state, we measured ^{19}F NMR spectra of ETM peptides containing either 4F-Phe20 or 4F-Phe26. ^{19}F chemical shifts are extremely sensitive to molecular conformation and dynamics[42, 48, 56–58]. We measured the ^{19}F CP spectra to preferentially detect rigid residues and DP spectra with a long recycle delay to provide more quantitative information about the relative concentrations of different species. Unexpectedly, both Phe20 and Phe26 exhibit two ^{19}F chemical shifts: a major peak A at −111 ppm and a minor peak B at −117 ppm (Fig. 3b, c). Thus, each Phe residue adopts two sidechain conformations. The peak doubling is observed at a range of P/L ratios (1:9 to 1:20) and in both purely fluorinated samples and mixed ^{13}C and ^{19}F labeled samples (Fig. S2c). Thus, the dual conformation of these two Phe sidechains is intrinsic to the peptide. Based on the intensities of the quantitative DP spectra, conformer A is dominant at neutral pH, representing ~60% of the total intensities, while at acidic pH with Ca^{2+}, conformer B becomes dominant, accounting for ~60% of the intensities. Peak B of Phe20 partially resolves into two peaks that are 1.0 ppm apart (Fig. 3b), suggesting small structural heterogeneity of this state. The peak B intensity is preferentially suppressed compared to peak A in the CP spectra, indicating that conformer B is more dynamic than conformer A. This dynamics is further manifested by the shorter ^{19}F T_1 relaxation time of conformer B compared to conformer A and by the preferential narrowing of peak B compared to peak A at low P/L (Fig. S2c, d). Taken together, these data indicate that both Phe20 and Phe26 exhibit two sidechain conformations: a rigid conformer A that dominates in the closed state of the channel and a dynamic conformer B that dominates in the open state. The fact that A and B intensities change with ion concentrations suggests that channel opening involves Phe sidechain conformational changes.

To assess whether the two sidechain conformations coexist in each channel or separated into different channels, we measured 2D ^{19}F-^{19}F correlation spectra using a 400 ms mixing time (Fig. 3d, e). Phe20 exhibits A-B cross peaks at 26 kHz MAS with CORD mixing, but no cross peaks at 38 kHz MAS with ^{1}H-driven spin diffusion (PDSD) (Fig. S6a, b). Since motionally induced exchange cross peaks do not depend on spinning frequency or the mixing method, the loss of the A-B cross peaks at faster MAS under PDSD mixing indicates that the cross peaks observed at slower MAS result from spin diffusion. Thus, the A and B conformers coexist within the same channel. We also measured the 2D FF spectrum at a lower P/L of 1:20 (Fig. S6b). The A-B cross peaks are reproduced, confirming that the A and B conformers are well mixed within each helical bundle. Based on the cross peak intensity buildup as a function of mixing time, we extracted the ^{19}F spin diffusion rate constant[50], which corresponds to an A-B distance of ~8.7 Å (Fig. S6c, d). Compared to Phe20, the Phe26 A and B conformers do not display correlation peaks under the same experimental conditions (Fig. 3e), indicating that the Phe26 sidechains are further apart from each other in the helical bundle.

The two Phe sidechain conformations are correlated with channel opening

To understand the nature of the two Phe sidechain conformations, we measured 2D ^{1}H-^{19}F and ^{13}C-^{19}F HETCOR spectra. The ^{1}H-^{19}F HETCOR spectra correlate water and lipid ^{1}H signals with the Phe ^{19}F signals to detect the water accessibility and lipid contact of the Phe sidechains. Fig. 4a shows a representative 2D ^{1}H-^{19}F HETCOR spectrum of 4F-Phe20 labeled ETM at pH 4.5 with Ca^{2+}. With 100 ms ^{1}H spin diffusion, 4F-Phe20 exhibits correlations with both water and lipid chain protons. But the relative intensities of these cross peaks differ between the A and B conformers. In the closed state, conformer A's water cross peak intensity is moderately enhanced compared to its CP intensity, whereas conformer B's lipid cross peak intensity is significantly higher than its CP intensity (Fig. 4b). These results (Fig. S7) indicate that conformer B preferentially interacts with lipid chains whereas conformer A is more accessible to the water-filled channel pore. The preferential water accessibility of conformer A compared to conformer B is more clearly seen for Phe20 than Phe26. Given the long spin diffusion mixing time of 100 ms, this result suggests that Phe20 conformer B ($Phe20_B$) is especially dehydrated. Compared to Phe20, Phe26 has higher lipid cross peaks for both A and B states, indicating that they are in closer contact with lipid chains than Phe20.

Importantly, ETM channel opening by acidic pH and calcium ions significantly increased the lipid cross peak intensity of $Phe20_B$ compared to the intensity in the closed state (Fig. 4c), indicating that $Phe20_B$ is in closer contact with lipids in the open state than in the closed state. Consistent with the 2D ^{1}H-^{19}F HETCOR spectra, ^{1}H-^{13}C HETCOR spectra show higher Phe sidechain cross peaks with lipids in the open state than in the closed state (Fig. S7c). These results, taken together, indicate that Phe20 and Phe26 sidechains exist in a conformational equilibrium between a lipid-facing B state and a water-accessible A state (Fig. 4d). Acidic pH and Ca^{2+} shift the equilibrium toward the lipid-facing state, and the change is more pronounced at Phe20 than at Phe26.

Complementing the ^{1}H-^{19}F HETCOR experiments, we measured 2D ^{13}C-^{19}F HETCOR spectra of 1 : 1 mixtures of ^{13}C,^{15}N-labeled ETM and fluorinated ETM to investigate interhelical packing of the Phe sidechains. For Phe20, we observed ^{13}C-^{19}F cross peaks between conformer A and the aromatic ^{13}C signals of Phe residues in neighboring helices for both the closed and open states (Fig. 5a). Thus, the Phe20 A conformer is in close contact with neighboring helices. In particular, we observed interhelical cross peaks between Phe20 ^{19}F and V24/V25 ^{13}C, and the peak intensities are higher in the open state than the closed state (Fig. 5a, Fig. S6e). The low-pH interhelical Phe20-Val24/25 contact is interesting, because a V25F mutation is known to inhibit the cation conduction of ETM[10–11]. This observation was previously interpreted as due to disruption of the oligomerization of ETM. Double V25F/A32F mutation restored channel conductance[16]. The NMR data shown here instead suggest that Val25 may affect the Phe20 sidechain conformational equilibrium to inhibit cation transport. The double mutation might counteract the perturbation by V25F, by restoring the coupled conformational equilibria at Phe20 and Phe26.

Compared to conformer A, the conformer B ^{19}F signal displays fewer ^{13}C cross peaks, indicating that the lipid-facing conformer B is further away from residues in the neighboring

helices. Between the closed and open states, conformer B shows higher ^{13}C-^{19}F cross peaks in the low-pH open state than the neutral-pH closed state. This can be explained by the low population of conformer B in the closed state.

While Phe20 exhibits various cross peaks with neighboring chains, the Phe26 interhelical ^{13}C-^{19}F cross peaks are weaker (Fig. 5b). This is consistent with the absence of Phe26 A-B ^{19}F-^{19}F cross peaks and suggests that the Phe26 sidechain is far from Phe20 and Phe23 in the same helix as well as in neighboring helices.

Discussion

Structural features of the open state of ETM

The solid-state NMR data shown here demonstrate that acidic pH and Ca^{2+} ions increase the water accessibility of the SARS-CoV-2 ETM pore and shift the sidechain conformational landscape of Phe20 and Phe26. By using a lysosome-mimetic pH of 4.5 and a calcium concentration that is sufficient to saturate the ETM channel, we probe the structural and dynamical response of ETM to these two cations. The 2D NCα and CC spectra (Fig. 2, Fig. S4) indicate that acidic pH and calcium ions perturb the conformations and increase the dynamics of the N- and C-terminal residues, and increase the water accessibility of the channel. The higher water accessibility is consistent with electrophysiological data that E-mediated current is increased by acidic pH and calcium[11, 13, 17]. The more hydrated open state has similar chemical shifts and hence similar backbone conformation as the closed state for the central portion of the TM domain, but has more disordered termini. This suggests that either the helices adopt the same monomer structure as the closed state but pack more loosely in the open state, or maintain similar pore diameters for the central portion of the channel but loosen at the two termini to yield increased water accessibility to the hydrophobic core. Acidic pH and calcium cause the same structural changes to ETM, indicating these changes cannot be attributed only to the protonation state of the unique acidic residue in the protein, E8. Instead, hydrogen bonding and salt bridge interactions at E8 and R38 are likely both involved in channel opening. The carbonyl region of 1D ^{13}C spectra at high and low pH (Fig. S4d) indicates that R38 CO and guanidinium Cζ are broadened at acidic pH with bound Ca^{2+}, whereas the E8 sidechain Cδ signal is only visible in the ^{13}C DP spectra, suggesting intermediate timescale dynamics. Additional studies are required to delineate the structure and dynamics of these terminal residues in the open state of ETM.

The Phe aromatic network model for ETM channel opening

The ^{19}F NMR spectra of Phe20 and Phe26 reveal an intricate aromatic network whose conformations correlate with, and possibly regulate, ETM channel opening. In both the neutral-pH Ca^{2+}-free sample and the low-pH Ca^{2+}-bound sample, Phe20 and Phe26 exhibit two sidechain conformations. These two conformers coexist in each channel, as evidenced by the A-B cross peaks in the 2D ^{19}F-^{19}F correlation spectra (Fig. 3). In the closed-state structure[42], the Phe20 and Phe 23 rings on each helix are 3.5–6.0 Å apart. This distance range[59] should allow π-π stacking within the same chain as well as potential van der Waals interactions between neighboring chains. Thus, Phe20 and Phe26 could rearrange

their sidechain conformations in a concerted manner in response to acidic pH and calcium binding. This sidechain conformational rearrangement is supported by the observed intensity changes of the two ^{19}F peaks with pH and calcium binding. At neutral pH, the water-facing A conformer is dominant, whereas at low pH with Ca^{2+}, the lipid-facing B conformer is dominant. Conformer A is in closer contact with residues on neighboring helices whereas conformer B is further away from residues in neighboring helices. Phe20's B conformation may also differ slightly between the closed and open states, as suggested by the different lipid cross peak intensities (Fig. 4b, c). The two sidechain conformations of Phe are resolved by ^{19}F NMR but not by ^{13}C NMR, as shown by 1D and 2D ^{13}C spectra of the protein at high and low pH (Fig. S8). The lack of ^{13}C spectral resolution is understandable, because Phe Cδ and Cε chemical shifts are highly overlapped and the presence of three Phe residues in the uniformly ^{13}C-labeled protein further cause spectral congestion. The ^{19}F spectral resolution for the singly fluorinated Phe residues thus showcases the ability of ^{19}F NMR spectra to provide detailed sidechain structural information that is difficult to obtain from ^{13}C NMR.

Based on these ^{19}F NMR data and the closed-state ETM structure, we propose the following model of the Phe sidechain conformations in the closed and open ETM (Fig. 6). We consider the Phe χ_1 angle, which can adopt three states, *trans (t)*, *gauche positive* (*p*) and *gauche negative* (*m*). The χ_2 angle of Phe residues is predominantly centered around $\pm 80^{\circ}$[60], and does not affect the position of the para-hydrogen that is replaced by ^{19}F here. For Phe20, the water-accessible conformer A can be achieved by a p90 rotamer whereas the lipid-facing conformer B can be achieved by a m-85 rotamer. The A state p90 rotamer would place the Phe20 fluorine near Phe23 and Val25 of the neighboring helix (Fig. 6c), which is consistent with the observed interhelical C-F correlations. For Phe26, the water-accessible A conformer can be achieved with a m-85 rotamer whereas the lipid-facing B conformer can be achieved with a t80 rotamer. With these sidechain rotamers, none of the Phe26-Phe26 A-A, A-B and B-B configurations give sufficiently short interhelical F-F and C-F distances to be detected. This is consistent with the absence of Phe26 cross peaks in the 2D ^{19}F-^{19}F spectra (Fig. 3e). If we assume that Phe20 and Phe26 in the same helix adopt the same conformer, either the water-accessible A state or the lipid-facing B state, then there are only three types of interhelical interfaces: AA, BA, and BB (Fig. 6c). The AA interface must exist in the closed state while the BB interface must exist in the open state. The AA interface, seen in the closed structure of ETM, contains a counter-directional arrangement of the Phe20 and Phe26 sidechains. This might hinder the loosening of the central portion of the helical bundle, thus restricting water and cation passage. In comparison, the BB interface, which allows the Phe sidechains to freely interact with lipids, neither constricts the helical bundle nor obstructs the pore lumen, thus favoring cation transport. The BA interface is present in both the closed and open states, and has more complex inter-chain interactions. Alternatively, the AA and BB structures might regulate cation transport via allosteric interactions between the Phe residues and other hydrophobic residues such as Val25. Such an allosteric mechanism might serve to couple the conformational changes of the two termini to the hydrophobic center of the TM domain. This model, although crude due to its assumption of the all-A or all-B conformations in each helix, is consistent with all experimental data available so far. If each helix adopts mixed A and B conformers for Phe20 and Phe26, then the aromatic network should endow the helical bundle with varying degrees of spaciousness along the

segment ^{20}FLA^{23}FVV^{26}F. Full structure determination of the open-state ETM, as well as direct measurement of the Phe23 conformation, will be necessary to further test this model and provide detailed insights into the opening mechanism of ETM.

This model depicts a complex and finely tuned aromatic network that can interact with key residues such as Val25. The close contact between Phe20 and Val25 in the open state seen in the 2D ^{13}C-^{19}F HETCOR spectra (Fig. 5a) is noteworthy, because V25F mutation is known to inhibit ion conductivity in ETM[10–11]. This inhibition was previously thought to be due to disruption of the oligomeric state of the E protein. However, a recent solution NMR study found that the V25F mutant of ETM does not cause significant CSPs, thus the oligomeric state is likely unchanged[36]. Instead, the Phe20-Val25 contact suggest that the V25F mutation may disrupt the finely tuned aromatic network by changing the Phe20 A-B conformational equilibrium, thus causing the channel to shift to the closed state.

Aromatic gating in other ion channels

Aromatic gating has been experimentally observed and computationally predicted for various viroporins and ion channels. In influenza A and B M2 proteins, the Trp residue in the functional HxxxW motif constitutes the gating residue, which achieves inward rectification of these proton channels[54, 61–65]. Between these two M2 proteins, SARS-CoV-2 ETM behaves more analogously to BM2 than AM2: ETM shows limited chemical shift changes between high and low pH, just like BM2[48, 66], while AM2 exhibits significant chemical shift changes between high and low pH. BM2 channel opening at low pH is accomplished by a widening of the pore and a slightly larger tilt angle of the helices, while the tertiary structure of each helix is unchanged. The hepatitis virus C p7 viroporin contains three Phe residues (Phe22, Phe25, and Phe26) in the center of the TM domain, whose joint mutations to Ala's significantly increased the channel activity, as shown by a liposome-based fluorescent dye assay[67]. Recently, homology modeling, water docking, lipid docking, and in-silico membrane insertion of E[22] were conducted based on the solution NMR structure of SARS-CoV-1 E in LMPG micelles[68]. This computational study found that the Phe26 sidechain points to the pore lumen in the closed state, thus forming a bottleneck of the channel. Water docking created an open state, in which the Phe26 sidechain changed its conformation and pointed away from the pore. This result is in qualitative agreement with the current ^{19}F NMR data of the coexistence of two sidechain conformations at both Phe20 and Phe26. The only difference is that the closed state structure of ETM indicates an interfacial orientation of Phe20 and Phe26. This interfacial orientation is consistent with the observed interhelical contacts as well as the water accessibility of these sidechains in the A state.

We speculate that the conformational equilibria of Phe20 and Phe26 might also play a role in the non-selectivity of the E channel. The different Phe rotamers could introduce structural plasticity to residues that are actively involved in cation conduction, thus enabling different ions to be transported. Such an effect was recently demonstrated for the non-selective NaK channel, which conducts both Na^+ and K^+ [69]. The selectivity filter of the NaK channel (TVGDG) differs from the selectivity filter of K^+ selective channels (TVGYG) by a single residue. The NaK selectivity filter exhibits two conformations that interchange on the μs-ms

timescale to shift the populations in response to different cations[69–70]. An extensive network of sidechains acts on the backbone of the selectivity filter, inducing different conformations.

In conclusion, the current solid-state NMR data provide molecular-level structural insights into the open state of the SARS-CoV-2 E protein in ERGIC-mimetic lipid bilayers. ETM transitions to a more water-accessible state at acidic pH and upon calcium binding. ^{19}F NMR spectra of sidechain fluorinated Phe's revealed an intricate aromatic network in the middle of the TM domain that correlates with the open and closed states of the channel. We hypothesize that this aromatic network might regulate the passage of water and cations through the channel pore either directly or indirectly by allosteric interactions with other residues. These results suggest that mutations of these Phe residues or small molecules that target this part of the E TM domain might be useful for inhibiting the E viroporin activity.

Supplementary Material

Refer to Web version on PubMed Central for supplementary material.

Acknowledgements

This work is supported by NIH grant GM088204 to M.H. J.M.S. gratefully acknowledges a Rubicon Fellowship 452020132 supported by the Dutch Research Council (NWO). J.M.S also acknowledges EMBO for supporting a Non-Stipendiary Postdoctoral Fellowship ALTF 1056-2020. This study made use of NMR spectrometers at the MIT-Harvard Center for Magnetic Resonance, which is supported by NIH grant P41 GM132079.

References

1. Boson B; Legros V; Zhou B; Siret E; Mathieu C; Cosset FL, … Denolly S, The SARS-CoV-2 envelope and membrane proteins modulate maturation and retention of the spike protein, allowing assembly of virus-like particles. J. Biol. Chem 2021, 296, 100111. [PubMed: 33229438]
2. Nieva JL; Madan V; Carrasco L, Viroporins: structure and biological functions. Nat. Rev. Microbiol 2012, 10, 563–74. [PubMed: 22751485]
3. Schoeman D; Fielding BC, Coronavirus envelope protein: current knowledge. Virol. J 2019, 16, 69. [PubMed: 31133031]
4. Corse E; Machamer CE, The cytoplasmic tails of infectious bronchitis virus E and M proteins mediate their interaction. Virology 2003, 312, 25–34. [PubMed: 12890618]
5. Baudoux P; Carrat C; Besnardeau L; Charley B; Laude H, Coronavirus pseudoparticles formed with recombinant M and E proteins induce alpha interferon synthesis by leukocytes. J. Virol 1998, 72, 8636–43. [PubMed: 9765403]
6. Jimenez-Guardeno JM; Nieto-Torres JL; DeDiego ML; Regla-Nava JA; Fernandez-Delgado R; Castano-Rodriguez C; Enjuanes L, The PDZ-binding motif of severe acute respiratory syndrome coronavirus envelope protein is a determinant of viral pathogenesis. PLoS Pathog. 2014, 10, e1004320. [PubMed: 25122212]
7. Chai J; Cai Y; Pang C; Wang L; McSweeney S; Shanklin J; Liu Q, Structural basis for SARS-CoV-2 envelope protein recognition of human cell junction protein PALS1. Nat. Commun 2021, 12, 3433. [PubMed: 34103506]
8. De Maio F; Lo Cascio E; Babini G; Sali M; Della Longa S; Tilocca B, … Urbani A, Improved binding of SARS-CoV-2 Envelope protein to tight junction-associated PALS1 could play a key role in COVID-19 pathogenesis. Microbes Infect. 2020, 22, 592–597. [PubMed: 32891874]
9. Shepley-McTaggart A; Sagum CA; Oliva I; Rybakovsky E; DiGuilio K; Liang J, … Harty RN, SARS-CoV-2 Envelope (E) protein interacts with PDZ-domain-2 of host tight junction protein ZO1. PLoS One 2021, 16, e0251955. [PubMed: 34106957]

10. Verdia-Baguena C; Nieto-Torres JL; Alcaraz A; DeDiego ML; Torres J; Aguilella VM; Enjuanes L, Coronavirus E protein forms ion channels with functionally and structurally-involved membrane lipids. Virology 2012, 432, 485–94. [PubMed: 22832120]
11. Nieto-Torres JL; Verdia-Baguena C; Jimenez-Guardeno JM; Regla-Nava JA; Castano-Rodriguez C; Fernandez-Delgado R, … Enjuanes L, Severe acute respiratory syndrome coronavirus E protein transports calcium ions and activates the NLRP3 inflammasome. Virology 2015, 485, 330–9. [PubMed: 26331680]
12. Cabrera-Garcia D; Bekdash R; Abbott GW; Yazawa M; Harrison NL, The envelope protein of SARS-CoV-2 increases intra-Golgi pH and forms a cation channel that is regulated by pH. J. Physiol 2021, 599, 2851–2868. [PubMed: 33709461]
13. Xia B; Shen X; He Y; Pan X; Liu FL; Wang Y, … Gao Z, SARS-CoV-2 envelope protein causes acute respiratory distress syndrome (ARDS)-like pathological damages and constitutes an antiviral target. Cell Res. 2021, 31, 847–860. [PubMed: 34112954]
14. Breitinger U; Ali NKM; Sticht H; Breitinger HG, Inhibition of SARS CoV Envelope Protein by Flavonoids and Classical Viroporin Inhibitors. Front. Microbiol 2021, 12, 692423. [PubMed: 34305855]
15. Toft-Bertelsen TL; Jeppesen MG; Tzortzini E; Xue K; Giller K; Becker S, … Rosenkilde MM, Amantadine has potential for the treatment of COVID-19 because it inhibits known and novel ion channels encoded by SARS-CoV-2. Commun. Biol 2021, 4, 1347. [PubMed: 34853399]
16. Torres J; Maheswari U; Parthasarathy K; Ng L; Liu DX; Gong X, Conductance and amantadine binding of a pore formed by a lysine-flanked transmembrane domain of SARS coronavirus envelope protein. Protein. Sci 2007, 16, 2065–71. [PubMed: 17766393]
17. Verdia-Baguena C; Nieto-Torres JL; Alcaraz A; Dediego ML; Enjuanes L; Aguilella VM, Analysis of SARS-CoV E protein ion channel activity by tuning the protein and lipid charge. Biochim. Biophys. Acta 2013, 1828, 2026–31. [PubMed: 23688394]
18. Paroutis P; Touret N; Grinstein S, The pH of the secretory pathway: measurement, determinants, and regulation. Physiology 2004, 19, 207–215. [PubMed: 15304635]
19. Ghosh S; Dellibovi-Ragheb TA; Kerviel A; Pak E; Qiu Q; Fisher M, … Altan-Bonnet N, β-Coronaviruses Use Lysosomes for Egress Instead of the Biosynthetic Secretory Pathway. Cell 2020, 183, 1520–1535.e14. [PubMed: 33157038]
20. Nieto-Torres JL; DeDiego ML; Verdia-Baguena C; Jimenez-Guardeno JM; Regla-Nava JA; Fernandez-Delgado R, … Enjuanes L, Severe acute respiratory syndrome coronavirus envelope protein ion channel activity promotes virus fitness and pathogenesis. PLoS Pathog. 2014, 10, e1004077. [PubMed: 24788150]
21. Xu Z; Shi L; Wang Y; Zhang J; Huang L; Zhang C, … Wang FS, Pathological findings of COVID-19 associated with acute respiratory distress syndrome. Lancet Respir. Med 2020, 8, 420–422. [PubMed: 32085846]
22. Sarkar M; Saha S, Structural insight into the role of novel SARS-CoV-2 E protein: A potential target for vaccine development and other therapeutic strategies. PLoS One 2020, 15, e0237300. [PubMed: 32785274]
23. Zumla A; Chan JF; Azhar EI; Hui DS; Yuen KY, Coronaviruses - drug discovery and therapeutic options. Nat. Rev. Drug. Discov 2016, 15, 327–47. [PubMed: 26868298]
24. DeDiego ML; Alvarez E; Almazan F; Rejas MT; Lamirande E; Roberts A, … Enjuanes L, A severe acute respiratory syndrome coronavirus that lacks the E gene is attenuated in vitro and in vivo. J. Virol 2007, 81, 1701–13. [PubMed: 17108030]
25. Fett C; DeDiego ML; Regla-Nava JA; Enjuanes L; Perlman S, Complete protection against severe acute respiratory syndrome coronavirus-mediated lethal respiratory disease in aged mice by immunization with a mouse-adapted virus lacking E protein. J. Virol 2013, 87, 6551–9. [PubMed: 23576515]
26. Watanabe S; Watanabe T; Kawaoka Y, Influenza A virus lacking M2 protein as a live attenuated vaccine. J. Virol 2009, 83, 5947–50. [PubMed: 19321619]
27. Liao Y; Yuan Q; Torres J; Tam JP; Liu DX, Biochemical and functional characterization of the membrane association and membrane permeabilizing activity of the severe acute respiratory syndrome coronavirus envelope protein. Virology 2006, 349, 264–75. [PubMed: 16507314]

28. Rahman MS; Hoque MN; Islam MR; Islam I; Mishu ID; Rahaman MM, … Hossain MA, Mutational insights into the envelope protein of SARS-CoV-2. Gene Rep. 2021, 22, 100997. [PubMed: 33319124]
29. Troyano-Hernaez P; Reinosa R; Holguin A, Evolution of SARS-CoV-2 Envelope, Membrane, Nucleocapsid, and Spike Structural Proteins from the Beginning of the Pandemic to September 2020: A Global and Regional Approach by Epidemiological Week. Viruses 2021, 13.
30. Julia L Mullen GT, Alaa Abdel Latif, Manar Alkuzweny, Marco Cano, Emily Haag, Jerry Zhou, Mark Zeller, Emory Hufbauer, Nate, Andersen Kristian G., Wu Chunlei, Su Andrew I., Gangavarapu Karthik, Hughes Laura D., and the Center for Viral Systems Biology, Outbreak.info. Outbreak.info: 2021.
31. Pinto LH; Holsinger LJ; Lamb RA, Influenza virus M2 protein has ion channel activity. Cell 1992, 69, 517–528. [PubMed: 1374685]
32. Hong M; DeGrado WF, Structural basis for proton conduction and inhibition by the influenza M2 protein. Protein Sci. 2012, 21, 1620–1633. [PubMed: 23001990]
33. Pinto LH; Lamb RA, Influenza virus proton channels. Photochem. Photobiol. Sci 2006, 5, 629–32. [PubMed: 16761092]
34. Cady SD; Luo WB; Hu F; Hong M, Structure and function of the influenza M2 proton channel. Biochemistry 2009, 48, 7356–7364. [PubMed: 19601584]
35. Wilson L; Gage P; Ewart G, Hexamethylene amiloride blocks E protein ion channels and inhibits coronavirus replication. Virology 2006, 353, 294–306. [PubMed: 16815524]
36. Park SH; Siddiqi H; Castro DV; De Angelis AA; Oom AL; Stoneham CA, … Opella SJ, Interactions of SARS-CoV-2 envelope protein with amilorides correlate with antiviral activity. PLoS Pathog. 2021, 17, e1009519. [PubMed: 34003853]
37. Pervushin K; Tan E; Parthasarathy K; Lin X; Jiang FL; Yu D, … Torres J, Structure and inhibition of the SARS coronavirus envelope protein ion channel. PLoS Pathog. 2009, 5, e1000511. [PubMed: 19593379]
38. Wang C; Takeuchi K; Pinto LH; Lamb RA, Ion channel activity of influenza A virus M2 protein: characterization of the amantadine block. J. Virol 1993, 67, 5585–5594. [PubMed: 7688826]
39. Balannik V; Wang J; Ohigashi Y; Jing X; Magavern E; Lamb RA, … Pinto LH, Design and pharmacological characterization of inhibitors of amantadine-resistant mutants of the M2 ion channel of influenza A virus. Biochemistry 2009, 48, 11872–11882. [PubMed: 19905033]
40. Cady SD; Schmidt-Rohr K; Wang J; Soto CS; Degrado WF; Hong M, Structure of the amantadine binding site of influenza M2 proton channels in lipid bilayers. Nature 2010, 463, 689–692. [PubMed: 20130653]
41. Stouffer AL; Acharya R; Salom D; Levine AS; Di Costanzo L; Soto CS, … DeGrado WF, Structural basis for the function and inhibition of an influenza virus proton channel. Nature 2008, 451, 596–599. [PubMed: 18235504]
42. Mandala VS; McKay MJ; Shcherbakov AA; Dregni AJ; Kolocouris A; Hong M, Structure and drug binding of the SARS-CoV-2 envelope protein transmembrane domain in lipid bilayers. Nat. Struct. Mol. Biol 2020, 27, 1202–1208. [PubMed: 33177698]
43. Simon MD; Heider PL; Adamo A; Vinogradov AA; Mong SK; Li X, … Pentelute BL, Rapid flow-based peptide synthesis. Chembiochem 2014, 15, 713–20. [PubMed: 24616230]
44. Böckmann A; Gardiennet C; Verel R; Hunkeler A; Loquet A; Pintacuda G, … Lesage A, Characterization of different water pools in solid-state NMR protein samples. J. Biomol. NMR 2009, 45, 319–327. [PubMed: 19779834]
45. Baldus M; Petkova AT; Herzfeld J; Griffin RG, Cross polarization in the tilted frame: assignment and spectral simplification in heteronuclear spin systems. Molecular Physics. 1998, 95, 1197–1207.
46. Hou G; Yan S; Trebosc J; Amoureux JP; Polenova T, Broadband homonuclear correlation spectroscopy driven by combined R2(n)(v) sequences under fast magic angle spinning for NMR structural analysis of organic and biological solids. J. Magn. Reson 2013, 232, 18–30. [PubMed: 23685715]

47. Dregni AJ; Duan P; Hong M, Hydration and Dynamics of Full-Length Tau Amyloid Fibrils Investigated by Solid-State Nuclear Magnetic Resonance. Biochemistry 2020, 59, 2237–2248. [PubMed: 32453948]
48. Mandala VS; Loftis AR; Shcherbakov AA; Pentelute BL; Hong M, Atomic structures of closed and open influenza B M2 proton channel reveal the conduction mechanism. Nat. Struct. Mol. Biol 2020, 27, 160–167. [PubMed: 32015551]
49. Helmus JJ; Jaroniec CP, Nmrglue: an open source Python package for the analysis of multidimensional NMR data. J. Biomol. NMR 2013, 55, 355–67. [PubMed: 23456039]
50. Roos M; Wang T; Shcherbakov AA; Hong M, Fast Magic-Angle-Spinning (19)F Spin Exchange NMR for Determining Nanometer (19)F-(19)F Distances in Proteins and Pharmaceutical Compounds. J. Phys. Chem. B 2018, 122, 2900–2911. [PubMed: 29486126]
51. Venkatagopalan P; Daskalova SM; Lopez LA; Dolezal KA; Hogue BG, Coronavirus envelope (E) protein remains at the site of assembly. Virology 2015, 478, 75–85. [PubMed: 25726972]
52. Kellokumpu S, Golgi pH, Ion and Redox Homeostasis: How Much Do They Really Matter? Front. Cell Dev. Biol 2019, 7, 93. [PubMed: 31263697]
53. Appenzeller-Herzog C; Hauri HP, The ER-Golgi intermediate compartment (ERGIC): in search of its identity and function. J. Cell. Sci 2006, 119, 2173–83. [PubMed: 16723730]
54. Williams JK; Tietze D; Lee M; Wang J; Hong M, Solid-State NMR Investigation of the Conformation, Proton Conduction, and Hydration of the Influenza B Virus M2 Transmembrane Proton Channel. J. Am. Chem. Soc 2016, 138, 8143–55. [PubMed: 27286559]
55. Huster D; Yao X; Hong M, Membrane Protein Topology Probed by 1H Spin Diffusion from Lipids Using Solid-State NMR Spectroscopy. J. Am. Chem. Soc 2002, 124, 874–883. [PubMed: 11817963]
56. Elkins MR; Bandara A; Pantelopulos GA; Straub JE; Hong M, Direct Observation of Cholesterol Dimers and Tetramers in Lipid Bilayers. J. Phys. Chem. B 2021, 125, 1825–1837. [PubMed: 33560844]
57. Shcherbakov AA; Hisao G; Mandala VS; Thomas NE; Soltani M; Salter EA, … Hong M, Structure and dynamics of the drug-bound bacterial transporter EmrE in lipid bilayers. Nat. Commun 2021, 12, 172. [PubMed: 33420032]
58. Shcherbakov AA; Roos M; Kwon B; Hong M, Two-dimensional (19)F-(13)C correlation NMR for (19)F resonance assignment of fluorinated proteins. J. Biomol. NMR 2020, 74, 193–204. [PubMed: 32088840]
59. Marsili S; Chelli R; Schettino V; Procacci P, Thermodynamics of stacking interactions in proteins. Phys. Chem. Chem. Phys 2008, 10, 2673–85. [PubMed: 18464982]
60. Lovell SC; Word JM; Richardson JS; Richardson DC, The penultimate rotamer library. Proteins: Structure, Function, and Genetics 2000, 40, 389–408.
61. Tang Y; Zaitseva F; Lamb RA; Pinto LH, The Gate of the Influenza Virus M2 Proton Channel Is Formed by a Single Tryptophan Residue. J. Biol. Chem 2002, 277, 39880–39886. [PubMed: 12183461]
62. Pinto LH; Dieckmann GR; Gandhi CS; Papworth CG; Braman J; Shaughnessy MA, … DeGrado WF, A functionally defined model for the M2 proton channel of influenza A virus suggests a mechanism for its ion selectivity. Proc. Natl. Acad. Sci. USA 1997, 94, 11301–11306. [PubMed: 9326604]
63. Hu F; Luo W; Hong M, Mechanisms of proton conduction and gating in influenza M2 proton channels from solid-state NMR. Science 2010, 330, 505–8. [PubMed: 20966251]
64. Mandala VS; Liao SY; Kwon B; Hong M, Structural Basis for Asymmetric Conductance of the Influenza M2 Proton Channel Investigated by Solid-State NMR Spectroscopy. J. Mol. Biol 2017, 429, 2192–2210. [PubMed: 28535993]
65. Kwon B; Roos M; Mandala VS; Shcherbakov AA; Hong M, Elucidating Relayed Proton Transfer through a His-Trp-His Triad of a Transmembrane Proton Channel by Solid-State NMR. J. Mol. Biol 2019, 431, 2554–2566. [PubMed: 31082440]
66. Mandala VS; Liao SY; Gelenter MD; Hong M, The Transmembrane Conformation of the Influenza B Virus M2 Protein in Lipid Bilayers. Sci. Rep 2019, 9, 3725. [PubMed: 30842530]

67. StGelais C; Foster TL; Verow M; Atkins E; Fishwick CW; Rowlands D, … Griffin S, Determinants of hepatitis C virus p7 ion channel function and drug sensitivity identified in vitro. J. Virol 2009, 83, 7970–81. [PubMed: 19493992]

68. Surya W; Li Y; Torres J, Structural model of the SARS coronavirus E channel in LMPG micelles. Biochim. Biophys. Acta 2018, 1860, 1309–1317.

69. Shi C; He Y; Hendriks K; de Groot BL; Cai X; Tian C, … Sun H, A single NaK channel conformation is not enough for non-selective ion conduction. Nat. Commun 2018, 9, 717. [PubMed: 29459730]

70. Hendriks K; Öster C; Shi C; Sun H; Lange A, Sodium Ions Do Not Stabilize the Selectivity Filter of a Potassium Channel. J. Mol. Biol 2021, 433, 167091. [PubMed: 34090923]

71. McClenaghan C; Hanson A; Lee SJ; Nichols CG, Coronavirus Proteins as Ion Channels: Current and Potential Research. Front. Immunol 2020, 11, 573339. [PubMed: 33154751]

72. Nieto-Torres JL; Dediego ML; Alvarez E; Jimenez-Guardeno JM; Regla-Nava JA; Llorente M, … Enjuanes L, Subcellular location and topology of severe acute respiratory syndrome coronavirus envelope protein. Virology 2011, 415, 69–82. [PubMed: 21524776]

73. Maeda J; Repass JF; Maeda A; Makino S, Membrane topology of coronavirus E protein. Virology 2001, 281, 163–9. [PubMed: 11277690]

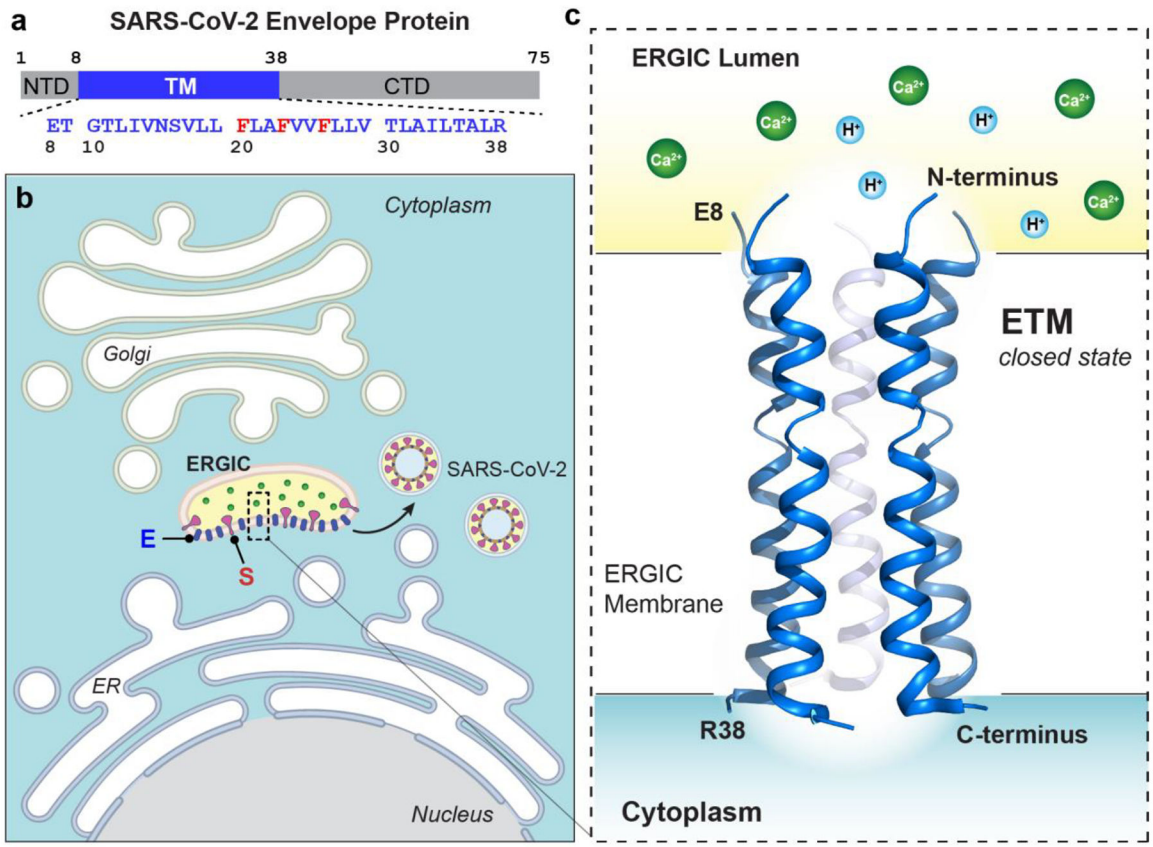

Figure 1.

(**a**) Amino acid sequence of the TM domain of SARS-CoV-2 envelope protein. The three Phe residues (red) are regularly spaced at Phe20, Phe23 and Phe26. (**b**) SARS-CoV-2 is assembled in the ERGIC, where the E protein is expressed in large quantities. E is involved in virus assembly and budding, interaction with other virus and host proteins, cation conduction, and activation of the inflammasome by altering cellular Ca^{2+} and H^{+} homeostasis[3, 71]. (**c**) The C terminus of ETM faces the cytoplasm while the N terminus faces the ERGIC lumen, which is acidic and rich in calcium[72–73]. The closed structure of ETM in lipid bilayers (PDB code: 7K3G) was solved recently using solid-state NMR[42].

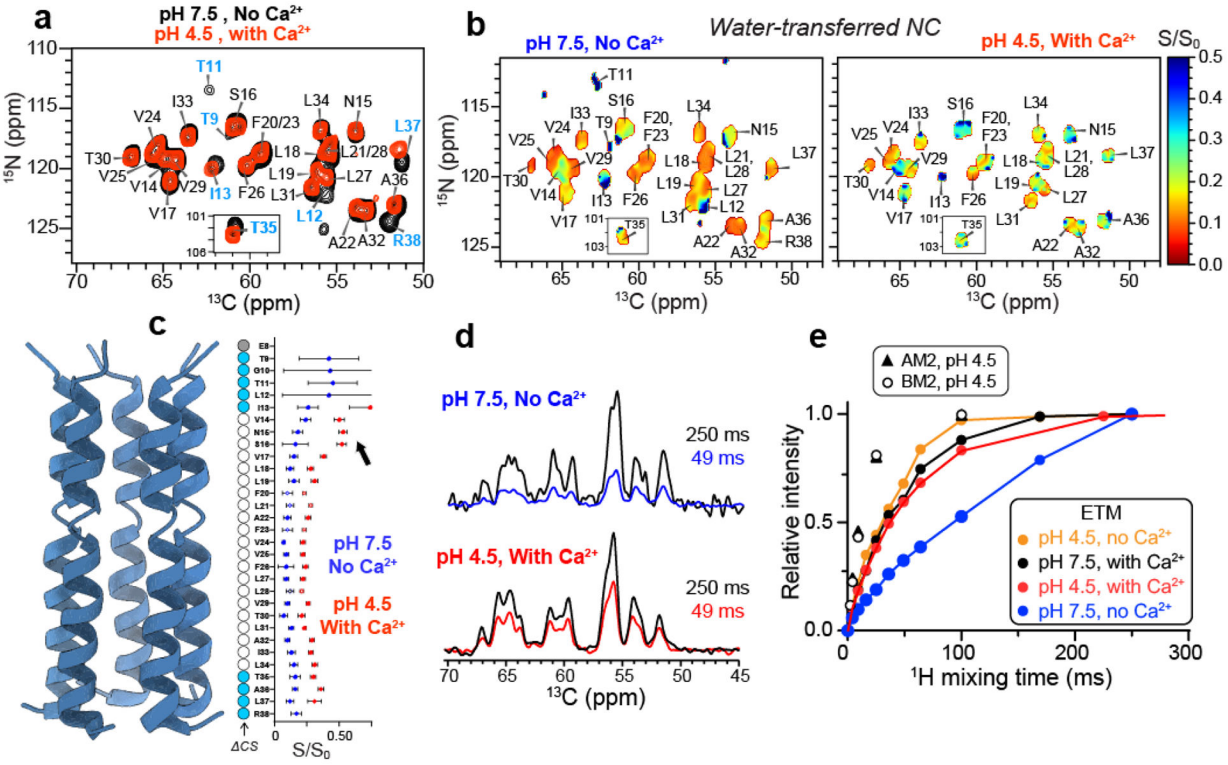

Figure 2.

Water-edited solid-state NMR spectra of membrane-bound ETM at different pH and Ca^{2+} concentrations. (**a**) 2D NCα spectrum of ETM at pH 7.5 without Ca^{2+} (black) and at pH 4.5 with Ca^{2+} (red). Resonance assignment is given. Blue assignments indicate residues with significant chemical shift perturbations. (**b**) Water-edited 2D NCα spectra of ETM at pH 7.5 without Ca^{2+} (left) and at pH 4.5 with Ca^{2+} (right). Contour colors denote the intensity ratios of spectra measured with 9 ms (S) and 100 ms (S_0) ^1H spin diffusion. Higher S/S_0 values indicate higher water accessibility. (**c**) Site-resolved water-transferred intensities obtained from the 2D NCα spectra of the neutral-pH sample (blue) and low-pH Ca^{2+}-bound sample (red). Open and closed symbols indicate overlapped and resolved peaks, respectively. Residues at the termini exhibit the largest hydration increase as well as the largest CSP (cyan circles) at acidic pH with Ca^{2+}. (**d**) Representative water-transferred 1D ^{15}N-^{13}C spectra at high pH and at acidic pH with Ca^{2+}. The relative intensity of the 49 ms spectrum to the 250 ms spectrum is lower in the neutral-pH sample than in the low-pH sample, indicating that the neutral-pH sample is less water accessible. (**e**) Water magnetization transfer buildup curves for ETM (colored symbols connected by lines) under four ionic conditions. The pH 7.5 no Ca^{2+} sample (blue) exhibits the slowest water magnetization transfer, while the pH 4.5 no Ca^{2+} sample (orange) exhibits the fastest water magnetization transfer. For comparison, AM2 and BM2 water buildup (open circles and filled triangles) at pH 4.5 is much faster than all the ETM samples.

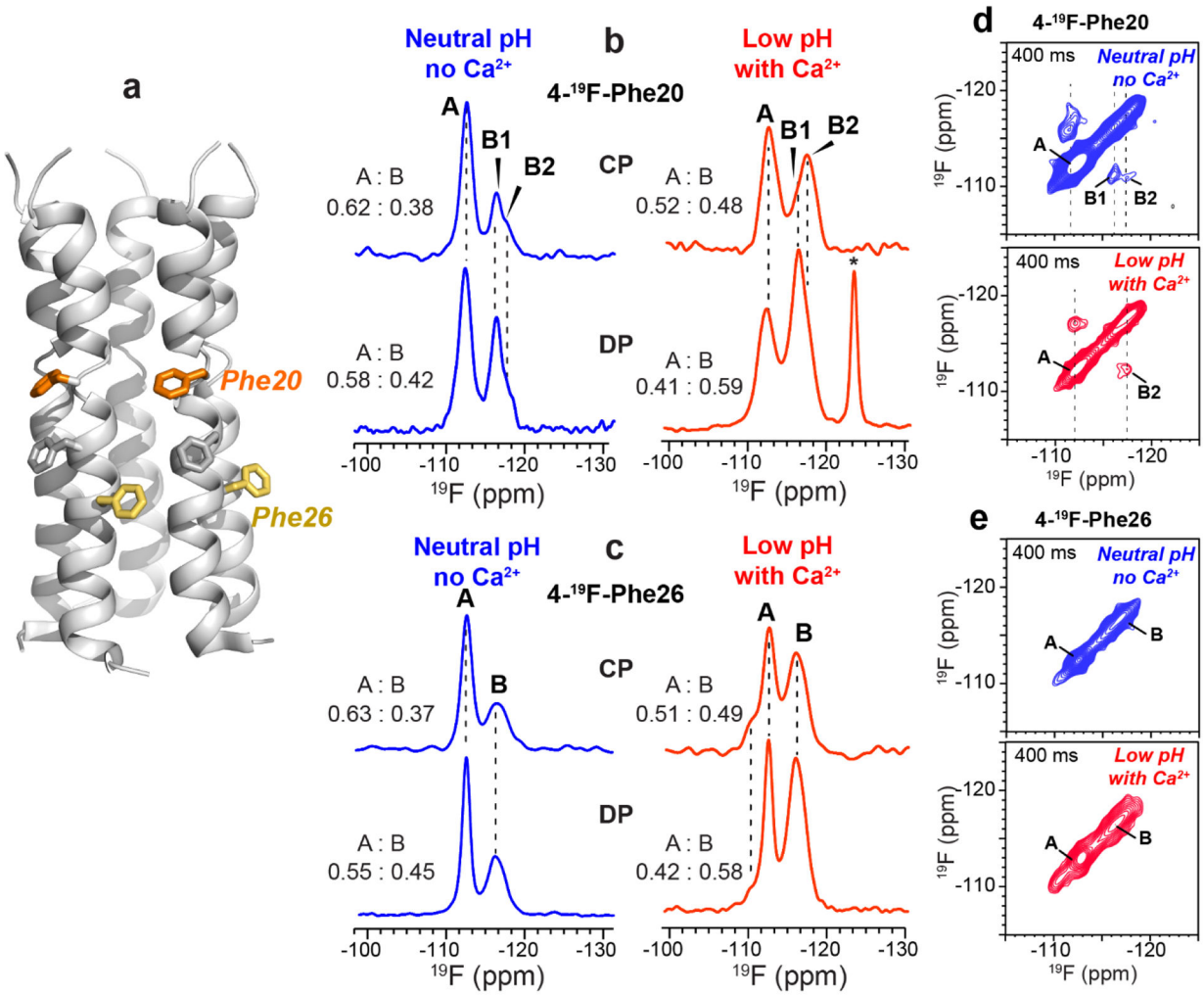

Figure 3.

^{19}F NMR spectra reveal two sidechain conformations of Phe20 and Phe26 in ETM. (**a**) Closed-state structure of ETM at neutral pH (PDB code: 7K3G). The positions of the three Phe residues are indicated. (**b**) ^{19}F CP and DP spectra of 4F-Phe20. (**c**) ^{19}F CP and DP spectra of 4F-Phe26. These ^{19}F spectra were measured at 290 K under 38 kHz MAS. The CP and DP spectra were measured with recycle delays of 1.5 s and 8 s, respectively. Both Phe20 and Phe26 show two ^{19}F peaks with varying intensity ratios. Asterisk (*) indicates a residual fluorine solvent peak. (**d**) 2D ^{19}F-^{19}F correlation spectra of 4F-Phe20 labeled ETM. (**e**) 2D ^{19}F-^{19}F correlation spectra of 4F-Phe26 labeled ETM. The spectra were measured with 400 ms CORD mixing under 26 kHz MAS. A-B cross peaks are observed for 4F-Phe20, indicating that A and B conformers coexist within each channel.

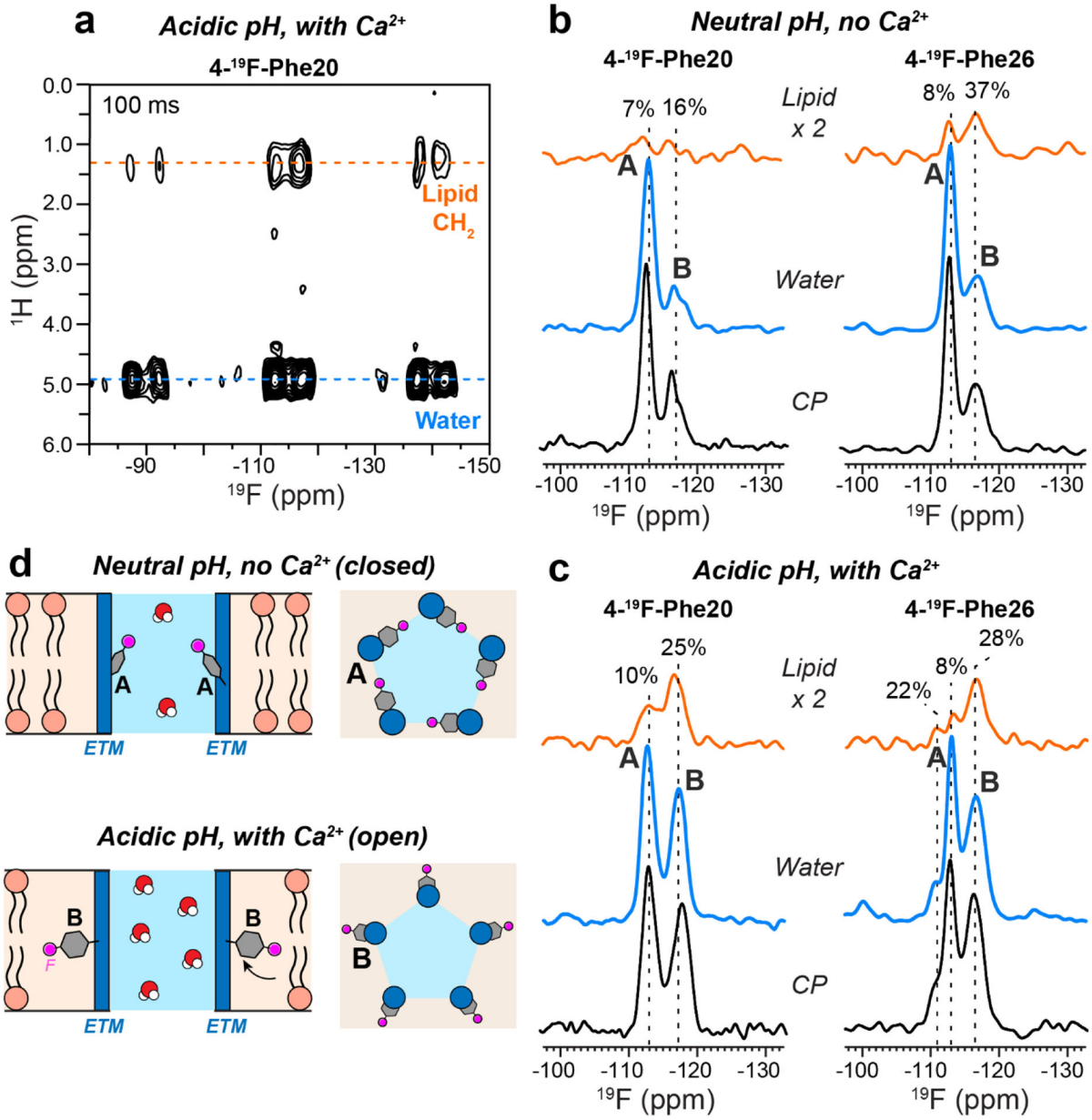

Figure 4.

^{1}H-^{19}F 2D HETCOR spectra to investigate water and lipid contacts with Phe sidechains. (**a**) A representative 2D HF HETCOR spectrum with 100 ms ^{1}H mixing, measured at 290 K under 14 kHz MAS. (**b**) Lipid and water ^{1}H cross sections of Phe20 and Phe26 in the closed state compared to the ^{19}F CP spectra. (**c**) Lipid and water ^{1}H cross sections of Phe20 and Phe26 in the open state. The relative intensities of the lipid cross peaks to the water cross peaks are given for each sample. Conformer B shows higher lipid cross peaks than conformer A as normalized by the CP intensities. (**d**) Schematic of conformer A, which is dominant in the closed state, and conformer B, which is dominant in the open state. For simplicity, only one conformer is shown in each channel, even though A and B conformers

coexist in each channel. Conformer B is more lipid facing whereas conformer A is more accessible to water in the pore.

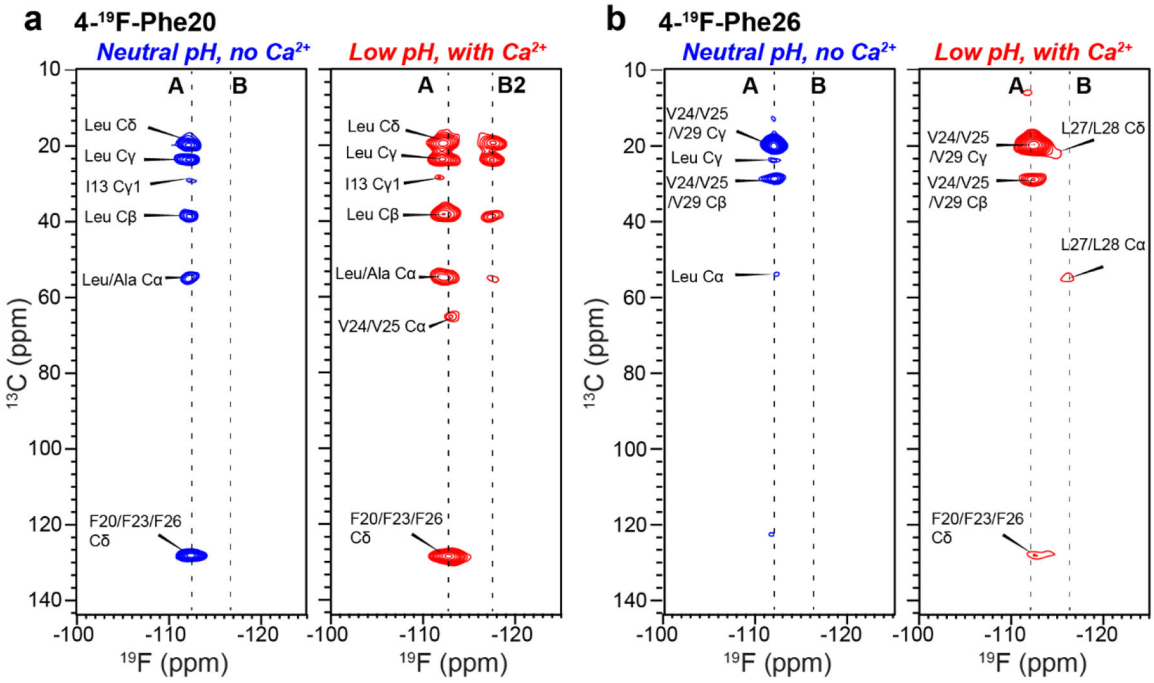

Figure 5.

2D ^{13}C-^{19}F HETCOR spectra of 1:1 mixed ^{13}C, ^{15}N-labeled ETM and 4F-Phe ETM at neutral pH (blue) and at low pH with Ca^{2+} (red). (**a**) 4F-Phe20 labeled ETM. (**b**) 4F-Phe26 labeled ETM. Conformer A shows more cross peaks with other residues than conformer B. The Phe20 sidechain shows more cross peaks than Phe26. The spectra were measured using 6 ms ^{13}C-^{19}F CP under 38 kHz MAS.

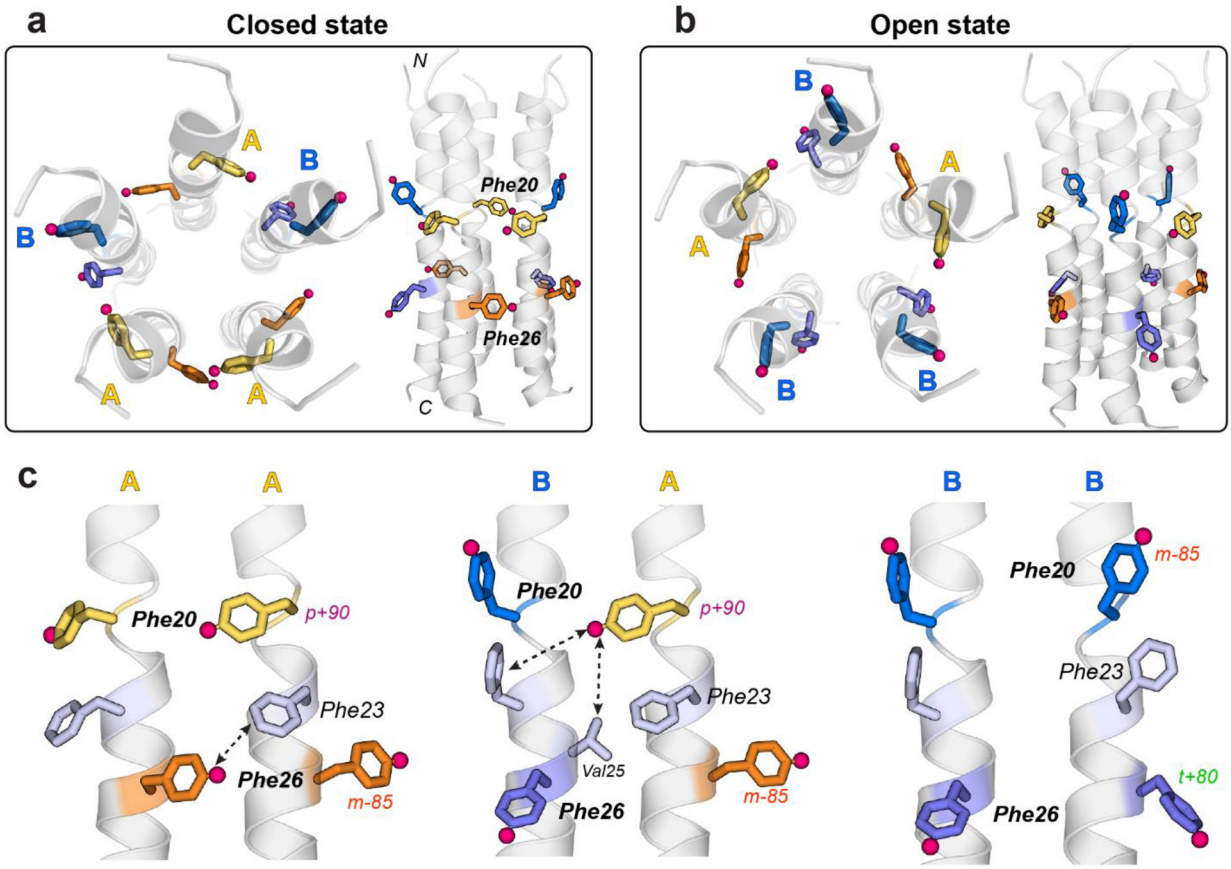

Figure 6.

Proposed model of the aromatic network of ETM, based on the backbone structure of the closed state of ETM (PDB: 7K3G). The Phe sidechains were reconstructed to satisfy the ^{19}F NMR spectra on the A and B conformer populations, the interhelical C-F and F-F contacts, and the water-peptide and lipid-peptide interactions in the closed and open channels. Pink spheres indicate fluorine. (**a**) Top and side views of the proposed Phe20 and Phe26 rotamers in the closed state. (**b**) Top and side views of the proposed Phe20 and Phe26 rotamers in the open state. (**c**) Model of the aromatic network for two ETM chains, showing AA, AB and BB rotamer combinations. The AA interface must exist in the closed channel whereas the BB interface must be present in the open channel. The mixed BA interface should be present in all channels.